Geophysical Research Letters

RESEARCH LETTER
10.1029/2019GL086706

Polar Amplification Due to Enhanced Heat Flux Across the Halocline

E. Beer[1], **I. Eisenman**[1], **and T. J. W. Wagner**[2]

[1]Scripps Institution of Oceanography, University of California San Diego, San Diego, CA, USA, [2]Department of Physics and Physical Oceanography, University of North Carolina at Wilmington, Wilmington, NC, USA

Key Points:
- We identify an oceanic mechanism that increases the vertical heat flux in the upper Arctic Ocean under global warming
- The enhanced heating occurs in regions with sea ice, and it causes increased ocean heat transport into the Arctic
- This mechanism is a substantial contributor to polar amplification in our model simulations

Supporting Information:
- Supporting Information S1

Correspondence to:
E. Beer,
ebeer@ucsd.edu

Citation:
Beer, E., Eisenman, I., & Wagner, T. J. W. (2020). Polar amplification due to enhanced heat flux across the halocline. *Geophysical Research Letters*, *47*, e2019GL086706. https://doi.org/10.1029/2019GL086706

Received 17 DEC 2019
Accepted 25 JAN 2020
Accepted article online 3 FEB 2020

Abstract Polar amplification is a widely discussed phenomenon, and a range of mechanisms have been proposed to contribute to it, many of which involve atmospheric and surface processes. However, substantial questions remain regarding the role of ocean heat transport. Previous studies have found that ocean heat transport into the Arctic increases under global warming, but the reasons behind this remain unresolved. Here, we investigate changes in oceanic heat fluxes and associated impacts on polar amplification using an idealized ocean-sea ice-climate model of the Northern Hemisphere. We show that beneath the sea ice, vertical temperature gradients across the halocline increase as the ocean warms, since the surface mixed layer temperatures in ice-covered regions are fixed near the freezing point. These enhanced vertical temperature gradients drive enhanced horizontal heat transport into the polar region and can contribute substantially to polar amplification.

Plain Language Summary The Arctic region is warming at a faster rate than the rest of the globe. A number of mechanisms that may contribute to this have been identified, the most well-known being the surface albedo feedback that occurs due to the higher reflectivity of ice compared to open water. However, substantial gaps remain in our understanding of what drives the polar amplification of global warming, and projections of how much the polar regions will warm in the future vary widely. Here, we look at the contribution to Arctic warming from the vertical transfer of heat in the upper ocean. In the Arctic Ocean, a large amount of heat is stored in relatively warm waters at depth, with a cold layer of water and sea ice cover above. The results indicate that the amount of heat from this warm water that reaches the sea ice cover will increase under global warming, enhancing the rate of warming in the Arctic region.

1. Introduction

Polar amplification is a robust feature of both observations and model projections in the Arctic region and of equilibrium global warming simulations in the Antarctic region (Collins et al., 2013; Holland & Bitz, 2003; Serreze et al., 2000). However, there is still substantial variability in the magnitude of polar amplification across models, and previous studies have proposed a range of different mechanisms as the main driver (Flato et al., 2013).

The surface albedo feedback (SAF) has been identified as the primary driver of polar amplification in some previous studies (Hall, 2004; Manabe & Wetherald, 1975; Manabe & Stouffer, 1980; Screen & Simmonds, 2010; Taylor et al., 2013). However, other processes have also been found to contribute substantially. The lapse rate feedback, which arises from vertical variations in atmospheric temperature changes and acts as a positive feedback in the Arctic and a negative feedback in lower latitudes, has been found in some studies to be the largest contributor to Arctic polar amplification (Goosse et al., 2018; Pithan & Mauritsen, 2014; Stuecker et al., 2018). The nonlinearity of the Planck feedback, which describes how warmer temperatures lead to more outgoing longwave radiation (OLR) due to the Stefan-Boltzmann law, causes there to be greater warming in cold high-latitude regions for the same increase in OLR and has also been found to be one of the main feedbacks contributing to polar amplification.

Other processes that have been suggested to play a role in polar amplification include increases in poleward heat transport in the atmosphere, changes in cloud cover, and increases in water vapor. Increases in poleward atmospheric heat transport tend to enhance polar amplification, although this can be dampened by other feedbacks (Alexeev & Jackson, 2013; Alexeev et al., 2005; Held & Soden, 2006; Hwang et al., 2011), whereas

changes in cloud cover can work as a positive or negative feedback depending on factors such as the time of year (Francis & Hunter, 2006; Kay & Gettelman, 2009; Schweiger et al., 2008). The water vapor feedback increases the level of global warming, but it is strongest in low latitudes and hence opposes polar amplification (Pithan & Mauritsen, 2014). Although these processes are typically thought to play a secondary role in the overall magnitude of polar amplification, they can be important when considering differences between climate models (Winton, 2006).

While previous research on polar amplification has focused mainly on the atmosphere, some studies using general circulation models (GCMs) have found increased northward ocean heat transport (OHT) into the Arctic Ocean under global warming (Bitz et al., 2006; Holland & Bitz, 2003; Hwang et al., 2011). These changes in OHT are largely consistent among GCMs, with a robust decrease in northward OHT in the mid-latitudes associated with a weakened overturning circulation, and a robust increase in OHT around 60–80° N (Hwang et al., 2011; Nummelin et al., 2017; van der Linden et al., 2019). Some studies of transient warming in GCMs have found that the ocean contributes to Arctic warming through this increased high-latitude OHT (Holland & Bitz, 2003; Mahlstein & Knutti, 2011) while other studies have found that the net effect of changes in OHT and ocean heat content opposes Arctic warming (Goosse et al., 2018; Pithan & Mauritsen, 2014). Nummelin et al. (2017) suggested that much of this discrepancy results from a focus on different latitude ranges and found that poleward of 75° N, changes in OHT were positively correlated with Arctic polar amplification. An increase in the temperature of Atlantic Water (AW) that flows into the Arctic Ocean has been suggested to contribute to the increase in OHT in GCMs (Bitz et al., 2006; Nummelin et al., 2017; van der Linden et al., 2019). Paleoproxy evidence also suggests an increase in AW temperature coinciding with Arctic polar amplification (Spielhagen et al., 2011). However, spatially-uniform ocean warming with unchanged circulation would cause warmer AW but no change in OHT, and the underlying physical mechanisms for the increase in OHT have remained unresolved.

In this study, we identify a mechanism by which the upward vertical oceanic heat flux under sea ice increases under global warming, with a corresponding increase in the horizontal OHT into the polar region. We demonstrate the mechanism using an idealized seasonally varying ocean-sea ice-climate model, which facilitates understanding of the underlying dynamics that could be at play in more complex models and also in the real world. We use a feedback-locking approach to show that changes in the vertical heat flux in the Arctic Ocean are a substantial contributor to polar amplification in the present simulations and drive increases in OHT that are comparable to those found in GCMs.

2. Idealized Ocean-Sea Ice-Climate Model

A depth profile for the Arctic Ocean is shown in Figure 1b. The upper Arctic Ocean can be characterized as consisting of a fresh and cold ocean surface mixed layer (SML) layer above a warmer AW layer, which is typically found to be below 200 m (Aagaard et al., 1981). The two layers are separated by a cold halocline layer of rapidly increasing salinity, which is highly stable and thereby limits the flux of heat from the AW up to the SML and the sea ice cover. We represent these features in an idealized model, which is sketched in Figure 1a. The two layers are fixed in depth to model the current climate's stratification of the SML and AW, where heat fluxes between the layers represent heat fluxes across the halocline. Note that there are regions where the local structure differs from this picture, such as the western Arctic Ocean where the stratification features an additional layer of Pacific water separating the SML from the AW (e.g., Timmermans et al., 2008).

This model builds on the model developed previously by Wagner and Eisenman (2015) (hereafter WE15), which has a single ocean layer representing the SML. WE15 combined the physics from idealized single-column model representations of thermodynamic sea ice processes (e.g., Eisenman & Wettlaufer, 2009; Eisenman, 2012) with that of energy balance models, or EBMs, of latitudinally and seasonally varying global surface temperature (e.g., Budyko, 1969; North, 1975; North & Coakley, 1979; Sellers, 1969). Here we add to this model a representation of a deeper ocean layer, somewhat analogous to previous idealized two-layer column models of the climate system (Gregory, 2000; Held et al., 2010). The deeper layer represents AW in the Arctic Ocean, and the two layers are coupled with a simple representation of the vertical heat flux that is proportional to the vertical temperature gradient, as shown in Figure 1a.

The upper layer in the model includes the ocean SML, sea ice, and the atmosphere above (Figure 1a). It is characterized by the surface enthalpy (E_s), which is a measure of the energy in the layer. We neglect the relatively small sensible heat contents of the atmosphere and of the sea ice and take E_s to be proportional to

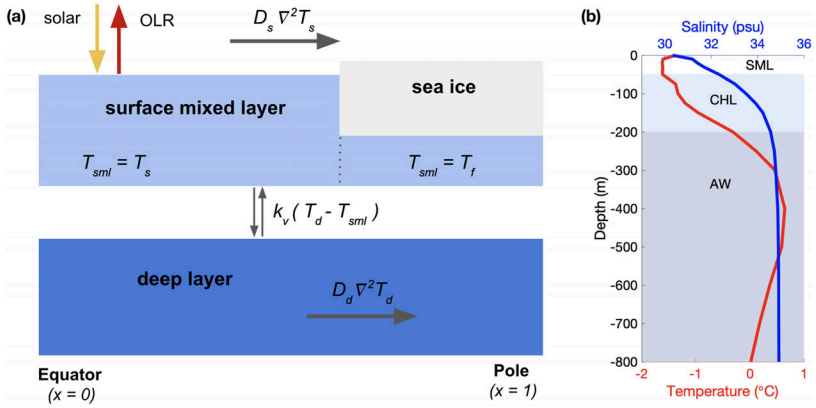

Figure 1. (a) Schematic of the idealized model, which represents the spatially and seasonally varying zonal-mean atmosphere, sea ice, ocean surface mixed layer (SML), and ocean deep layer in the Northern Hemisphere. The energy flux terms described in the main text are indicated, and T_s, T_d, and T_f represent the surface temperature, ocean deep layer temperature, and freezing point, respectively. The ocean SML temperature, T_{sml}, is set to the surface temperature in ice-free locations and the freezing point where sea ice is present. (b) Annual-mean observed depth profiles in the Arctic Ocean, averaged horizontally over 80–90° N, for temperature (red) and salinity (blue) (Levitus et al., 1994; Levitus & Boyer, 1994). The shading indicates the approximate depth ranges of three levels: the modeled SML, the cold halocline layer (CHL) separating the model layers, and the modeled deep layer, which represents Atlantic Water (AW) in the Arctic.

the SML temperature (T_{sml}) referenced to the freezing point (T_f) where no ice is present and proportional to the sea ice thickness (h) where ice is present:

$$E_s \equiv \begin{cases} -L_f\, h & E_s < 0, \\ c_s\,(T_{sml} - T_f) & E_s > 0. \end{cases} \tag{1}$$

In the deep layer we define a similar enthalpy, which is simply proportional to the deep layer temperature, T_d:

$$E_d = c_d\,(T_d - T_f). \tag{2}$$

Here, L_f is the sea ice latent heat of fusion, and $c_s \equiv \rho\, c_p\, H_s$ and $c_d \equiv \rho\, c_p\, H_d$ are the heat capacities for the surface and deep ocean layers, respectively, with H_s the depth of the SML, H_d the depth of the deep layer, ρ the seawater density, and c_p the seawater specific heat capacity. The freezing point, T_f, is fixed in the model. Where there is no ice, the SML temperature is equal to the surface temperature (T_s), but where ice is present, it is taken to remain at the freezing point:

$$T_{sml} = \begin{cases} T_s & E_s > 0, \\ T_f & E_s < 0. \end{cases} \tag{3}$$

The enthalpy E_s at each horizontal location in the layer evolves in response to the top-of-atmosphere incident solar radiation S scaled by the coalbedo a, which is defined as one minus the albedo; OLR, which is treated as a linear function of surface temperature T_s with parameters A and B; meridional heat transport in the atmosphere, which is parameterized as diffusion of the surface temperature with constant coefficient D_s; vertical heat flux between the SML and the deep layer, which is parameterized as a down-gradient heat flux with coefficient k_v; and a climate forcing term F, which can represent changes in atmospheric CO_2:

$$\frac{\partial E_s}{\partial t} = \underbrace{a\,S}_{\text{solar}} - \underbrace{[A + B\,(T_s - T_f)]}_{\text{OLR}} + \underbrace{D_s \nabla^2 T_s}_{\text{horizontal flux}} + \underbrace{k_v\,(T_d - T_{sml})}_{\text{vertical flux}} + \underbrace{F}_{\text{forcing}}. \tag{4}$$

In the deep layer, horizontal heat transport is parameterized as diffusion of the ocean temperature with coefficient D_d, leading to

$$\frac{\partial E_d}{\partial t} = \underbrace{D_d \nabla^2 T_d}_{\text{horizontal flux}} + \underbrace{k_v\,(T_{sml} - T_d)}_{\text{vertical flux}}. \tag{5}$$

Where $E_s < 0$, equation (4) describes the evolution of sea ice thickness. To find the surface temperature, we approximate a linear temperature profile within the ice between the surface at temperature T_0 and the base at the freezing point T_f. We define T_0 as the surface temperature that would cause the vertical heat flux through the ice to be balanced by the surface flux terms (as in equation (4)) to give

$$\underbrace{k\,(T_f - T_0)/h}_{\text{heat flux through ice}} = -\underbrace{a\,S}_{\text{solar}} + \underbrace{[A + B\,(T_0 - T_f)]}_{\text{OLR}} - \underbrace{D_s \nabla^2 T_s}_{\text{horizontal flux}} - \underbrace{F}_{\text{forcing}}, \tag{6}$$

where k is the sea ice thermal conductivity. If this balance (6) leads to $T_0 < T_f$, then the ice is freezing. Otherwise, the ice is melting, and the surface of the ice is fixed at the freezing point. Hence, the three cases for the surface temperature are

$$T_s = \begin{cases} T_f + E_s/c_s, & E_s > 0, & \text{(open water)}, \\ T_f, & E_s < 0, T_0 > T_f, & \text{(melting ice)}, \\ T_0, & E_s < 0, T_0 < T_f, & \text{(freezing ice)}. \end{cases} \tag{7}$$

The model accounts for converging meridians on the Earth by using the Laplacian operator for polar variations in spherical coordinates for the horizontal diffusion in the surface and deep layers,

$$\nabla^2 = \frac{\partial}{\partial x}\left[(1 - x^2)\frac{\partial}{\partial x}\right], \tag{8}$$

with $x \equiv \sin\theta$ with θ the latitude. The coalbedo a is included with an empirically motivated representation for ice-covered ($E_s < 0$) and ice-free ($E_s > 0$) conditions,

$$a = \begin{cases} a_0 - a_2 x^2 & E_s > 0, \\ a_i & E_s < 0, \end{cases}, \tag{9}$$

and the solar radiation varies with latitude and season as

$$S = S_0 - S_1 x \cos\omega t - S_2 x^2 \tag{10}$$

with $\omega = 2\pi$ year^{-1}. The model domain is the Northern Hemisphere, and we approximate the heat flux across the equator to be zero, which gives the boundary conditions

$$\left.\frac{\partial E_s}{\partial x}\right|_{x=0} = 0, \quad \left.\frac{\partial E_d}{\partial x}\right|_{x=0} = 0. \tag{11}$$

These representations are equivalent to WE15 for the SML, sea ice, and atmospheric meridional heat transport, but we add a deeper ocean layer in the present model and replace the specified constant heat flux into the base of the SML in WE15 with the computed flux $k_v(T_d - T_{sml})$. This adds two new parameters, the horizontal diffusion coefficient in the deep layer D_d and the vertical heat flux coefficient k_v. Slight changes have been made to the parameters used in WE15 to better fit observations using the present model. The determination of the parameter values is described in Text S1 in the supporting information, which draws on a number of additional previous studies (Davis et al., 2016; Nummelin et al., 2015; Peterson et al., 2017; Polyakov et al., 2017; Polyakov et al., 2018; Reigstad et al., 2002). A list of the parameter values is given in Table S1, and the model simulation results for the control climate are presented alongside observational estimates in Figure 2.

Although the model domain stretches from the equator to the North Pole, our focus is on the Arctic. The SML depth is set to 50 m, which has been used in previous idealized models of the Arctic (e.g., Thorndike, 1992), although observed mixed layer depths vary widely. The deep layer depth is set to 600 m, corresponding to a depth range of 200–800 m, which broadly characterizes the AW beneath the cold halocline in the Arctic Ocean (e.g., Carmack et al., 2015). Outside the Arctic this layer crudely represents the ocean thermocline, although the simulated temperature in this layer does not agree well with observations of this depth range in the tropics (Figures 2b and 2e), where colder temperatures are associated with equatorial upwelling, which is not represented in this model. The two layers are indicated in the Arctic Ocean depth profiles in Figure 1b.

The model takes several centuries to fully spin up. We analytically calculate the approximate e-folding timescales of the surface and deep layer to be 1.6 and 77 years, respectively (see Text S2 and Figure S1). All plotted simulation results were spun up for a minimum of 2,000 years.

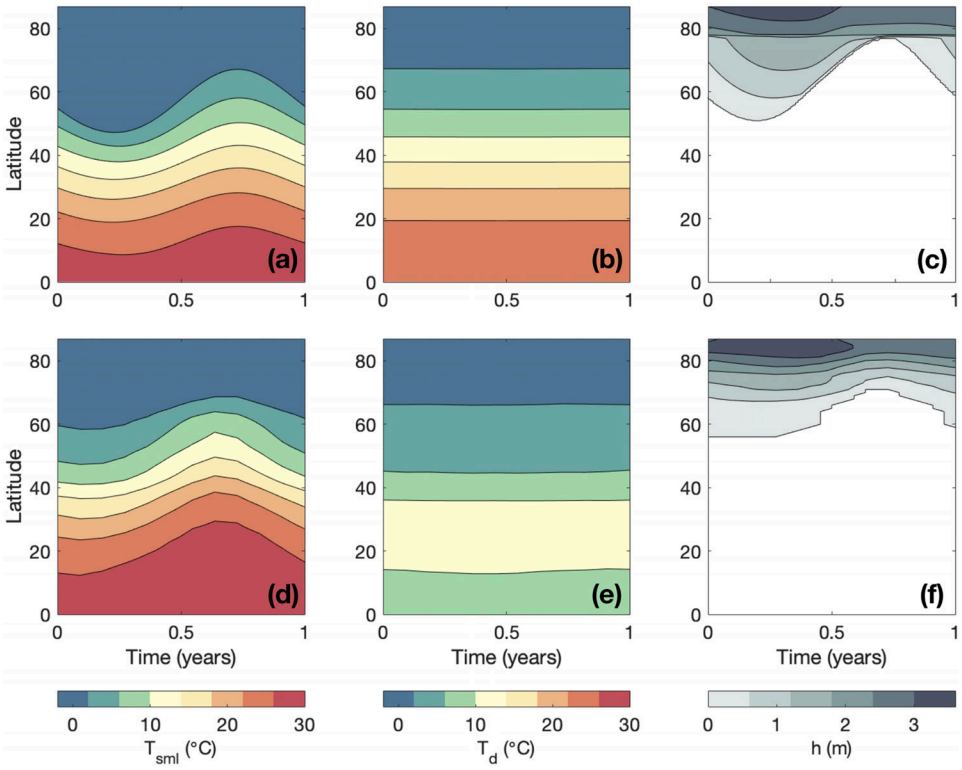

Figure 2. Idealized model results compared with observations. The top three panels are output for the final year of a model simulation with default parameter values, showing (a) the ocean SML temperature, (b) the ocean deep layer temperature, and (c) the sea ice thickness. The bottom three panels show observational estimates for comparison: (d) the zonal-mean 1950–1993 mean climatological sea surface temperature (Reynolds & Smith, 1995), (e) the 1900–1992 mean climatological ocean temperature averaged zonally and over the depth range 200–800 m (Levitus & Boyer, 1994), and (f) the zonal-mean 1979–2000 mean climatological sea ice thickness omitting grid boxes with less than 15% ice concentration (Zhang & Rothrock, 2003).

3. Results

In this model, the vertical heat flux from the deep ocean to the ice is proportional to the temperature difference between the SML temperature (T_{sml}) and the deep layer temperature (T_d). Since the SML temperature is set to the freezing point (T_f) in regions of sea ice cover, rather than having the colder surface temperature, there is a relatively small temperature gradient between the SML and warmer Arctic deep layer, leading to a relatively small upward vertical heat flux across the halocline.

We simulate global warming in the model by increasing the climate forcing parameter F, which can be interpreted to represent an increase in atmospheric CO_2. We increase F abruptly and then run the model until it is spun up at a new, warmer state. At locations where sea ice remains present, the warming results in a thinner ice cover but the SML temperature remains at the freezing point. Since the deep ocean layer warms, this results in an increase in the vertical heat flux, amplifying the warming in regions with sea ice cover. This is demonstrated in Figure 3a, where midwinter temperatures for the SML and deep layer are shown for $F = 0$ W m^{-2} (default value, dashed lines) and for $F = 10$ W m^{-2} (solid lines). This relatively large change in climate forcing is used here to more clearly show the difference between the climates.

The change in the vertical heat flux is spatially dependent on the location of the ice edge. Since the ice edge moves throughout the year, this means the spatial difference in heat flux will change seasonally. This is illustrated for midwinter and midsummer in Figure S2, where plots of the vertical heat flux at $F = 0$ and $F = 3$ W m^{-2} reveal a slight decrease in the vertical heat flux at the initial ice edge (left side of dashed red line) and the greatest increase at the new ice edge (left side of solid red line).

Next, we investigate how this change in vertical heat flux affects the level of polar amplification in the model. This idealized model only feels the effect of one of the processes mentioned in the introduction that could

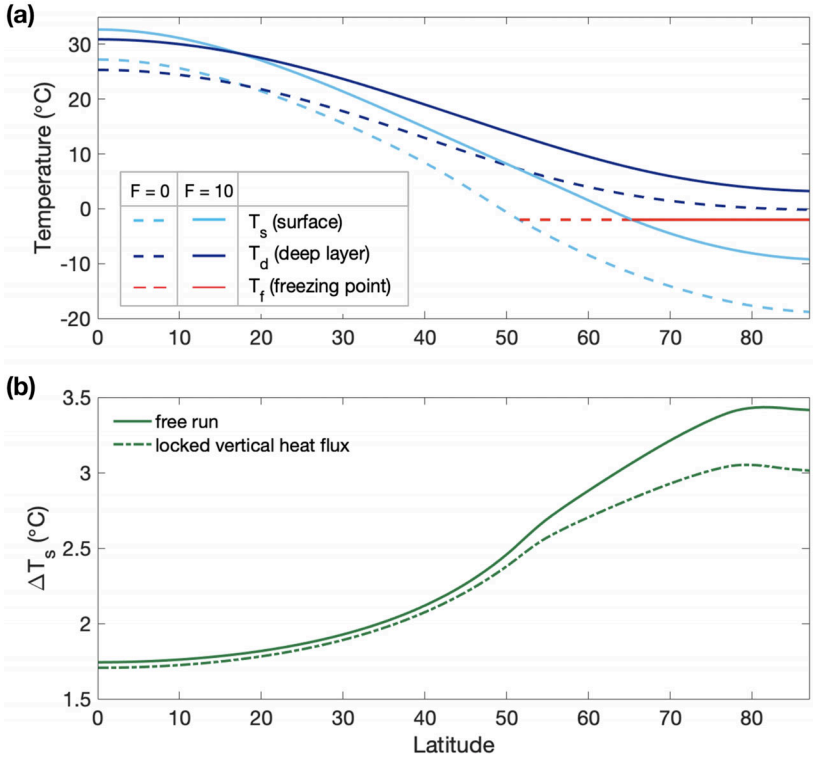

Figure 3. (a) Temperature variations between the equator and pole at midwinter ($t = 0.25$). Model results with $F = 0$ W m^{-2} are plotted as dashed lines and results with $F = 10$ W m^{-2} are plotted as solid lines. The surface temperature is indicated in light blue and the deep layer temperature in dark blue. The freezing point, which is the minimum allowed SML temperature, is indicated in red. This figure illustrates that as the temperature increases under forced warming (from dashed to solid lines), the difference between the deep layer temperature (dark blue) and SML temperature that is fixed at the freezing point in locations with sea ice (red) increases at high latitudes, leading to an increase in the vertical flux upward into the SML. (b) Annual-mean surface temperature difference between simulated climates with climate forcing set at $F = 0$ and $F = 3$ W m^{-2}. The solid green line indicates the results from the model in its standard configuration. The dash-dotted line indicates the case with the vertical heat flux locked to match the field simulated in the run with $F = 0$ W m^{-2}.

contribute to polar amplification, the SAF, as well as the oceanic heating mechanism that is the focus of this study.

We adopt as the definition of the polar amplification factor

$$\mathrm{PA} \equiv \frac{\overline{\Delta T_{s,\mathrm{polar}}}}{\overline{\Delta T_{s,\mathrm{NH}}}}, \tag{12}$$

where $T_{s,\mathrm{polar}}$ is the surface temperature averaged over 70–90° N and $T_{s,\mathrm{NH}}$ is the surface temperature averaged over 0–90° N, the bar denotes the annual mean, and Δ indicates the change between two climates. Note that a range of polar amplification factor definitions have been used in previous studies (as reviewed in Hind et al., 2016).

In Figure 3b, we plot the change in surface temperature when F is increased from 0 to 3 W m^{-2}. This increase can be compared with the radiative forcing from doubling of CO_2, which is estimated to be 3.7 W m^{-2} with a range of ±20% (Collins et al., 2013). Note however that because this idealized model lacks the water vapor feedback and other processes, the hemispheric-mean temperature in the model warms by 2 ° C in response to this increase in F, compared with equilibrium climate sensitivities to doubling CO_2 in GCMs, which typically fall in the range 3.2 ± 1.3 ° C (Flato et al., 2013).

We lock the feedback associated with changes in the vertical heat flux across the halocline by replacing the vertical flux term in equation (4) by a specified seasonally varying and latitudinally varying field that is equal to the field simulated with the default value of $F = 0$ W m^{-2}. Previous studies have used similar

feedback-locking methods to evaluate the strength of the SAF by keeping the surface albedo field fixed while the ice retreats under global warming (Cess et al., 1991; Hall, 2004; Graversen & Wang, 2009). Figure 3b shows temperature variations in simulations with the vertical heat flux locked (dash-dotted green line) compared with free runs (solid green line) that have the vertical heat flux evolve as the climate warms according to equation (4). The polar amplification factor in the locked case is $PA_{locked} = 1.45$, and in the free case, it is $PA_{free} = 1.55$. Note that the locked vertical heat flux version of the model is equivalent to a one-layer model with a prescribed heat flux into the bottom. We calculate the contribution to polar amplification by the vertical heat flux as follows (Graversen et al., 2014):

$$PA_{contribution} = \frac{PA_{free} - PA_{locked}}{PA_{free} - 1}. \quad (13)$$

The result in Figure 3b is $PA_{contribution} = 0.2$. In other words, the contribution to polar amplification from enhanced heat flux across the halocline in the idealized model is 20%. Note that the remaining polar amplification in the model is due to the SAF, since only the SAF and the enhanced vertical heat flux contribute to polar amplification in this idealized model. This is demonstrated with further feedback-locking simulations in Figure S3, where a small amount of polar amplification can be seen in simulations when the surface albedo is locked but the vertical heat flux is free to evolve, but no polar amplification occurs when both the surface albedo and vertical heat flux are locked. Other processes contributing to polar amplification that are not included in the model, such as the lapse rate feedback, could complicate these results.

Nonetheless, the idealized model results can be compared with previous GCM simulations that showed an increase in high-latitude OHT under warming. In a direct test of how this impacts Arctic warming, Singh et al. (2017) found that changes in ocean heat flux convergence in a GCM contributes 23% to Arctic amplification over ocean regions under CO_2 doubling, although a physical mechanism was not identified. This result is similar to the idealized model result of 20% in the present study, which is directly attributable to the mechanism proposed here. The increase in OHT found in this idealized model can also be compared with GCMs. Hwang et al. (2011) found that 9 out of the 10 GCMs they analyzed simulated increased OHT at 70° N under warming, with the OHT per degree of global warming falling between 0.001 and 0.03 PW (under the SRES "A2" scenario). The idealized model result falls within this range, with a increase of 0.007 PW at 70° N per degree of hemispheric warming. The change in OHT for a simulation with the idealized model that undergoes 2° C of hemispheric-mean warming is shown in Figure S4.

4. Discussion

In Figure 3b the free run has a larger increase in global-mean temperature than the run with a locked vertical heat flux. This occurs due to the interaction between the two processes that drive polar amplification in the model: Changes in vertical heat flux influence the sea ice cover and hence the albedo. Further feedback-locking simulations demonstrate that due to these interactions, polar amplification from the enhanced heat fluxes alone plus that due to the SAF alone is smaller than the polar amplification when both processes occur (see Figure S3). Hence, the result $PA_{contribution} = 0.2$ represents a combination of the contribution from changes to the vertical heat flux and the nonlinear contribution from interactions between the vertical heat flux and the surface albedo. The highest contribution from the SAF occurs near the ice edge, which explains why the maximum temperature change in Figure 3b occurs at approximately 80° N rather than at the pole.

The ocean heat flux mechanism presented here acts to enhance the temperature response to both positive and negative climate forcing anywhere that sea ice is present (and the ocean temperature increases with depth). This is in contrast to the SAF, which enhances changes only in locations where the sea ice cover changes. Both processes are hence expected to contribute to polar amplification of warming in climates resembling the present day or warmer, with sea ice residing in much of the Arctic Ocean. However, the results are expected to differ for climates with the ice edge residing outside of the Arctic. We explore the sensitivity to these factors by varying the initial and final values of F (see Figures S5 and S6). We find that when the Arctic becomes ice free in the summer, the contribution to polar amplification of the proposed mechanism and the SAF both decrease, and when the Arctic Ocean becomes ice free throughout the year, neither mechanism contributes and the model has no polar amplification, as expected. The results of colder simulated climates are discussed in Text S3.

This mechanism is proposed as a possible explanation for the increase in polar OHT in GCM simulations of greenhouse-driven warming. However, it should be emphasized that the model we use to demonstrate the mechanism has idealized diffusive representations of horizontal and vertical ocean heat fluxes, and aspects of the complex ocean circulation and heat transport simulated in GCMs that are not captured by this idealized representation could also contribute to the increase in simulated OHT. One indicator of the proposed mechanism that could be used to help identify whether it is occurring in GCM simulations would be to examine the spatial structure of changes in the vertical heat flux, since the mechanism notably causes an increase in the heat flux across the base of the ocean mixed layer in a given season only in locations that have sea ice in both the initial and final state (as shown in Figures 3a and S2). This would be expected to be most readily identifiable in GCM simulations of the equilibrium response to CO_2 increases.

All simulations in this study were run to approximate equilibrium, and the caveat should be noted that transient climates could behave differently. In an equilibrium state, ocean heat uptake is zero, but in a transient state, some studies have found that increases in ocean heat uptake oppose polar amplification (Goosse et al., 2018; Pithan & Mauritsen, 2014).

Although the model presented here is focused on Arctic regions where the lower layer represents AW, the proposed mechanism could apply to any warm water mass resting below ice. In ice-covered regions in the Western Arctic, it has been observed that halocline waters at depths of around 50–150 m are heating up faster than the surrounding waters. Since the surface waters under sea ice remain near the freezing point, the mechanism presented here may be expected to cause increased upward heat fluxes into the SML (cf. Timmermans et al., 2018). The proposed mechanism could also play a role in the Antarctic, where relatively warm circumpolar deep water resides below a fresher, cooler SML. Antarctic amplification is seen in some GCM simulations of the equilibrium response to increasing greenhouse forcing. Such GCM simulations have found that OHT increases in the polar regions of both hemispheres, although cloud changes in the Southern Hemisphere may compete with this effect (Singh et al., 2017).

5. Summary

This study presents a mechanism by which changes in the vertical heat flux across the halocline in the Arctic Ocean cause an increase in OHT into the Arctic, amplify sea ice retreat, and contribute to polar amplification. We demonstrate the mechanism using an idealized model of the Northern Hemisphere atmosphere, sea ice, ocean SML, and deeper ocean waters. The mechanism hinges on the surface water beneath the sea ice being fixed near the freezing point. When the climate warms, the deep water warms while surface waters under sea ice remain near the freezing point, which leads to an increase in the vertical temperature gradient and hence also an increase in the vertical heat flux from the deep waters to the surface waters. This enhances the warming in any regions that have sea ice and have subsurface waters that are warmer than the surface waters, as is the case in much of the Arctic Ocean.

This increase in vertical heat flux in the Arctic region necessitates an increase in the horizontal heat flux into the Arctic deep ocean layer. Such an increase in OHT under global warming has been noted previously in GCM simulations, but the physical mechanism has remained elusive. The mechanism presented here may provide an explanation for this behavior.

We use a feedback-locking approach to suppress the influence of vertical heat flux changes and thereby quantify the contribution of the proposed mechanism to polar amplification. The results show that changes in the vertical heat flux contribute 20% to polar amplification in the idealized model. This result is similar to previous GCM simulations, which tested the influence of changes in ocean heat flux convergence on Arctic amplification under global warming (Singh et al., 2017).

Previous work has identified a process by which atmospheric heat transport into the polar regions fundamentally increases under warming due to latent heat effects and the Clausius-Clapeyron relationship (Alexeev et al., 2005; Held & Soden, 2006). This work suggests that there is also a process by which OHT into the Arctic increases under warming due to changes in the vertical heat flux in the ocean.

Acknowledgments
Many thanks to Effie Fine, Marion Alberty, Jen Mackinnon, and Shantong Sun for helpful discussions and also to two anonymous reviewers for helpful comments. This work was supported by National Science Foundation Grant OPP-1643445. The code to numerically solve the model is available on GitHub: https://eisenman-group.github.io (doi:10.5281/zenodo.3628886). The observational data used in Figures 1 and 2 was downloaded online (from http://iridl.ldeo.columbia.edu and https://pscfiles.apl.uw.edu/zhang/PIOMAS).

References

Aagaard, K., Coachman, L. K., & Carmack, E. (1981). On the halocline of the Arctic Ocean. *Deep-Sea Research Part A-Oceanographic Research Papers*, *28*(6), 529–648.

Alexeev, V. A., & Jackson, C. H. (2013). Polar amplification: Is atmospheric heat transport important? *Climate Dynamics*, *41*(2), 533–547.

Alexeev, V. A., Langen, P. L., & Bates, J. R. (2005). Polar amplification of surface warming on an aquaplanet in "ghost forcing" experiments without sea ice feedbacks. *Climate Dynamics*, *24*(7-8), 655–666.

Bitz, C. M., Gent, P. R., Woodgate, R. A., Holland, M. M., & Lindsay, R. (2006). The influence of sea ice on ocean heat uptake in response to increasing CO2. *Journal of Climate*, *19*(11), 2437–2450.

Budyko, M. (1969). Effect of solar radiation variations on climate of Earth. *Tellus*, *21*(5), 611–619.

Carmack, E., Polyakov, I., Padman, L., Fer, I., Hunke, E., Hutchings, J., et al. (2015). Toward quantifying the increasing role of oceanic heat in sea ice loss in the new Arctic. *Bulletin of the American Meteorological Society*, *96*(12), 2079–2105.

Cess, R. D., Potter, G. L., Zhang, M. H., Blanchet, J. P., Chalita, S., Colman, R., et al. (1991). Interpretation of snow-climate feedback as produced by 17 general-circulation models. *Science*, *253*(5022), 888–892.

Collins, M., Knutti, R., Arblaster, J., Dufresne, J.-L., Fichefet, T., Friedlingstein, P., et al. (2013). Long-term climate change: Projections, commitments and irreversibility. In T. F. Stocker, D. Qin, G.-K. Plattner, et al. (Eds.), *Climate Change 2013: The Physical Science Basis. Contribution of Working Group I to the Fifth Assessment Report of the Intergovernmental Panel on Climate Change* (pp. 1029–1136). Cambridge, United Kingdom and New York, NY, USA: Cambridge University Press. www.climatechange2013.org

Davis, P. E. D., Lique, C., Johnson, H. L., & Guthrie, J. D. (2016). Competing effects of elevated vertical mixing and increased freshwater input on the stratification and sea ice cover in a changing Arctic Ocean. *Journal of Physical Oceanography*, *46*(5), 1531–1553.

Eisenman, I. (2012). Factors controlling the bifurcation structure of sea ice retreat. *Journal of Geophysical Research*, *117*, D01111. https://doi.org/10.1029/2011JD016164

Eisenman, I., & Wettlaufer, J. S. (2009). Nonlinear threshold behavior during the loss of Arctic sea ice. *Proceedings of the National Academy of Sciences of the United States of America*, *106*(1), 28–32.

Flato, G., Marotzke, J., Abiodun, B., Braconnot, P., Chou, S. C., Collins, W., et al. (2013). Evaluation of climate models. In T.F. Stocker, D. Qin, G.-K. Plattner, et al. (Eds.), *Climate Change 2013: The Physical Science Basis. Contribution of Working Group I to the Fifth Assessment Report of the Intergovernmental Panel on Climate Change* (pp. 741–866). Cambridge, United Kingdom and New York, NY, USA: Cambridge University Press. www.climatechange2013.org

Francis, J. A, & Hunter, E. (2006). New insight into the disappearing Arctic sea ice. *Eos, Transactions American Geophysical Union*, *2006*(46), 509–511.

Goosse, H., Kay, J. E., Armour, K. C., Bodas-Salcedo, A., Chepfer, H., Docquier, D., et al. (2018). Quantifying climate feedbacks in polar regions. *Nature Communications*, *9*, 1919.

Graversen, R. G., Langen, P. L., & Mauritsen, T. (2014). Polar amplification in CCSM4: Contributions from the lapse rate and surface albedo feedbacks. *Journal of Climate*, *27*(12), 4433–4450.

Graversen, R. G., & Wang, M. (2009). Polar amplification in a coupled climate model with locked albedo. *Climate Dynamics*, *33*(5), 629–643.

Gregory, J. M. (2000). Vertical heat transports in the ocean and their effect an time-dependent climate change. *Climate Dynamics*, *16*(7), 501–515.

Hall, A. (2004). The role of surface albedo feedback in climate. *Journal of Climate*, *17*(7), 1550–1568.

Held, I. M., & Soden, B. J. (2006). Robust responses of the hydrological cycle to global warming. *Journal of Climate*, *19*(21), 5686–5699.

Held, I. M., Winton, M., Takahashi, K., Delworth, T., Zeng, F., & Vallis, G. K. (2010). Probing the fast and slow components of global warming by returning abruptly to preindustrial forcing. *Journal of Climate*, *23*(9), 2418–2427.

Hind, A., Zhang, Q., & Brattstrom, G. (2016). Problems encountered when defining Arctic amplification as a ratio. *Scientific Reports*, *6*, 30469.

Holland, M. M., & Bitz, C. M. (2003). Polar amplification of climate change in coupled models. *Climate Dynamics*, *21*(3-4), 221–232.

Hwang, Y.-T., Frierson, D. M. W., & Kay, J. E. (2011). Coupling between Arctic feedbacks and changes in poleward energy transport. *Geophysical Research Letters*, *38*, L17704. https://doi.org/10.1029/2011GL048546

Kay, J. E., & Gettelman, A. (2009). Cloud influence on and response to seasonal Arctic sea ice loss. *Journal of Geophysical Research*, *114*, D18204. https://doi.org/10.1029/2009JD011773

Levitus, S., & Boyer, T. P. (1994). World Ocean Atlas 1994. Volume 4. Temperature.

Levitus, S., Burgett, R., & Boyer, T. P. (1994). World Ocean Atlas 1994. Volume 3. Salinity.

Mahlstein, I., & Knutti, R. (2011). Ocean heat transport as a cause for model uncertainty in projected arctic warming. *Journal of Climate*, *24*(5), 1451–1460.

Manabe, S., & Stouffer, R. J. (1980). Sensitivity of a global climate model to an increase of CO2 concentration in the atmosphere. *Journal of Geophysical Research*, *85*(NC10), 5529–5554.

Manabe, S., & Wetherald, R. T. (1975). Effects of doubling CO2 concentration on climate of a general circulation model. *Journal of the Atmospheric Sciences*, *32*(1), 3–15.

North, G. (1975). Theory of energy-balance climate models. *Journal of the Atmospheric Sciences*, *32*(11), 2033–2043.

North, G., & Coakley, J. (1979). Differences between seasonal and mean annual energy-balance model calculations of climate and climate sensitivity. *Journal of the Atmospheric Sciences*, *36*(7), 1189–1204.

Nummelin, A., Li, C., & Hezel, P. J. (2017). Connecting ocean heat transport changes from the midlatitudes to the Arctic Ocean. *Geophysical Research Letters*, *44*, 1899–1908. https://doi.org/10.1002/2016GL071333

Nummelin, A., Li, C., & Smedsrud, L. H. (2015). Response of Arctic Ocean stratification to changing river runoff in a column model. *Journal of Geophysical Research: Oceans*, *120*, 2655–2675. https://doi.org/10.1002/2014JC010571

Peterson, A. K., Fer, I., McPhee, M. G., & Randelhoff, A. (2017). Turbulent heat and momentum fluxes in the upper ocean under Arctic sea ice. *Journal of Geophysical Research: Oceans*, *122*, 1439–1456. https://doi.org/10.1002/2016JC012283

Pithan, F., & Mauritsen, T. (2014). Arctic amplification dominated by temperature feedbacks in contemporary climate models. *Nature Geoscience*, *7*(3), 181–184.

Polyakov, I. V., Pnyushkov, A. V., Alkire, M. B., Ashik, I. M., Baumann, T. M., Carmack, E. C., et al. (2017). Greater role for Atlantic inflows on sea-ice loss in the Eurasian Basin of the Arctic Ocean. *Science*, *356*(6335), 285+.

Polyakov, I. V., Pnyushkov, A. V., & Carmack, E. C. (2018). Stability of the Arctic halocline: A new indicator of Arctic climate change. *Environmental Research Letters*, *13*(12), 125008.

Reigstad, M., Wassmann, P., Riser, C. W., Oygarden, S., & Rey, F. (2002). Variations in hydrography, nutrients and chlorophyll a in the marginal ice-zone and the central Barents Sea. *Journal of Marine Systems*, *38*(1-2), 9–29.

Reynolds, R. W., & Smith, T. M. (1995). A high-resolution global sea-surface temperature climatology. *Journal of Climate*, *8*(6), 1571–1583.
Schweiger, A. J., Lindsay, R. W., Vavrus, S., & Francis, J. A. (2008). Relationships between Arctic sea ice and clouds during autumn. *Journal of Climate*, *21*(18), 4799–4810.
Screen, J. A., & Simmonds, I. (2010). The central role of diminishing sea ice in recent Arctic temperature amplification. *Nature*, *464*(7293), 1334–1337.
Sellers, W. D. (1969). A global climatic model based on the energy balance of the Earth-atmosphere system. *Journal of Applied Meteorology*, *8*(3), 392–400.
Serreze, M. C., Walsh, J. E., Chapin, F. S., Osterkamp, T., Dyurgerov, M., Romanovsky, V., et al. (2000). Observational evidence of recent change in the northern high-latitude environment. *Climatic Change*, *46*(1-2), 159–207.
Singh, H. A., Rasch, P. J., & Rose, B. E. J. (2017). Increased ocean heat convergence into the high latitudes with CO2 doubling enhances polar-amplified warming. *Geophysical Research Letters*, *44*, 10,583–10,591. https://doi.org/10.1002/2017GL074561
Spielhagen, R. F., Werner, K., Sorensen, S. A., Zamelczyk, K., Kandiano, E., Budeus, G., et al. (2011). Enhanced modern heat transfer to the Arctic by warm Atlantic Water. *Science*, *331*(6016), 450–453.
Stuecker, M. F., Bitz, C. M., Armour, K. C., Proistosescu, C., Kang, S. M., Xie, S.-P., et al. (2018). Polar amplification dominated by local forcing and feedbacks. *Nature Climate Change*, *8*(12), 1076–1081.
Taylor, P. C., Cai, M., Hu, A., Meehl, G. A., Washington, W., & Zhang, G. J. (2013). A decomposition of feedback contributions to polar warming amplification (vol 26, pg 7023, 2013). *Journal of Climate*, *26*(21), 8706.
Thorndike, A. (1992). A toy model linking atmospheric thermal-radiation and sea ice growth. *Journal of Geophysical Research*, *97*(C6), 9401–9410.
Timmermans, M.-L., Toole, J., & Krishfield, R. (2018). Warming of the interior Arctic Ocean linked to sea ice losses at the basin margins. *Science Advances*, *4*(8), eaat6773.
Timmermans, M. L., Toole, J., Krishfield, R., & Winsor, P. (2008). Ice-tethered profiler observations of the double-diffusive staircase in the Canada Basin thermocline. *Journal of Geophysical Research: Oceans*, *113*, C00A02. https://doi.org/10.1029/2008JC004829
van der Linden, E. C., Le Bars, D., Bintanja, R., & Hazeleger, W. (2019). Oceanic heat transport into the Arctic under high and low CO2 forcing. *Climate Dynamics*, *53*(7-8), 4763–4780.
Wagner, T. J. W., & Eisenman, I. (2015). How climate model complexity influences sea ice stability. *Journal of Climate*, *28*(10), 3998–4014.
Winton, M. (2006). Amplified Arctic climate change: What does surface albedo feedback have to do with it? *Geophysical Research Letters*, *33*, L03701. https://doi.org/10.1029/2005GL025244
Zhang, J. L., & Rothrock, D. A. (2003). Modeling global sea ice with a thickness and enthalpy distribution model in generalized curvilinear coordinates. *Monthly Weather Review*, *131*(5), 845–861.

Supporting Information for "Polar amplification due to enhanced heat flux across the halocline"

E. Beer[1], I. Eisenman[1], and T. J. W. Wagner[2]

[1]Scripps Institution of Oceanography, University of California San Diego, USA
[2]Department of Physics and Physical Oceanography, University of North Carolina Wilmington, USA

Contents of this file

1. Text S1 to S3
2. Figures S1 to S7
3. Table S1

Text S1. Determining Model Parameter Values.

The model developed in the present study has two new parameters in addition to the parameters in the previous model of Wagner and Eisenman (2015): the horizontal diffusion coefficient in the deep layer D_d and the vertical heat flux coefficient k_v. Some changes have also been made here to the parameter values used in Wagner and Eisenman (2015). These include shifting the freezing point (T_f) from 0 °C to −2 °C, which approximates the actual value for the salinities of 31 to 36 psu that are typically found in the Arctic Ocean (see Fig. 1b in the main text) and thereby better facilitates comparison with observations (Fig. 2 in the main text). The atmospheric diffusion coefficient D_s, solar cycle amplitude S_1, and OLR parameter A are also adjusted slightly from the values in WE15 to better fit observations using the present model (see bottom row of Fig. 2 in the main text). All parameter values are given in Table S1.

For the new parameters, the value of D_d is chosen to match observed temperature profiles and observations of horizontal heat transport. It gives an annual-mean northward OHT across 70 °N divided by the area poleward of 70 °N of 4.8 Wm^{-2}, which is consistent with observations that the northward heat transport by AW through Fram Strait contributes a basin-averaged flux to the Arctic Ocean of 5 ± 1 Wm^{-2} (Carmack et al., 2015). The value $k_v = 2$ W m^{-2} K^{-1} is chosen to give an observationally consistent seasonal cycle in ice thickness. Note that this value for k_v is similar to the value of 1.6 W m^{-2} K^{-1} used for a similar parameter in the column model of the global climate of Gregory (2000), which has upper and lower layer thicknesses of 150 m and 2400 m, respectively. The vertical flux averaged annually and over 70–90 °N in the control climate simulated in the model is 4.8 Wm^{-2}, which is within the observed range of vertical flux for the Eastern Arctic Ocean of 1–5 Wm^{-2} (Carmack et al., 2015; Peterson et al., 2017; Polyakov et al., 2017).

The values of these two parameters are expected to influence the contribution to polar amplification from the proposed mechanism, because they control how much heat gets transported into the deep Arctic Ocean and then up to the Arctic Ocean surface. In the model, k_v and D_d are set to constant values to best match the current climate. However, some observations and model results suggest that making these parameters dependent on the background climate state could possibly be more accurate. For example, the surface freshwater flux into the Arctic Ocean is predicted to increase under global warming in the future leading to enhanced stratification (Nummelin et al., 2015; Davis et al., 2016), which would be associated with a decrease in k_v. On the other hand, observations during recent decades suggest that there has been a shoaling of the AW as part of "atlantification", which is a term that describes how some characteristics of the Arctic Ocean are becoming more like the North Atlantic

(Reigstad et al., 2002; Polyakov et al., 2017, 2018), and this would be associated with an increase in k_v due to a weaker halocline layer insulating the AW from the SML.

Sensitivity to changes in the constant values of both of these parameters are explored in Fig. S7, where increases in either parameter are shown to result in an increase in the importance of the vertical heat flux mechanism for polar amplification.

It should be noted that since this model has many parameters, there may be another set of parameter values where the climate looks similar but responds differently to climate forcing.

Text S2. Analytical Estimate of Model Time Scales.

The transient evolution of the idealized model can be characterized by two timescales. The behavior is simplest when conditions are ice-free everywhere, which is the case we initially consider here. In this case we can make the simplifications that the surface enthalpy everywhere is proportional to the surface temperature ($E_s = c_s T_s$), the coalbedo (a) depends only on latitude, and the surface mixed layer temperature everywhere is equal to the surface temperature ($T_{sml} = T_s$). Taking the global mean of equations (3) and (4) in the main text, we find,

$$c_s \frac{d\overline{T_s}}{dt} = \overline{a\,S} - A - B\,(\overline{T_s} - T_f) + k_v\,(\overline{T_d} - \overline{T_s}) + F \tag{S1}$$

and

$$c_d \frac{d\overline{T_d}}{dt} = k_v\,(\overline{T_s} - \overline{T_d}), \tag{S2}$$

where bars denote averages over both the hemisphere and the year. To separate the timescales between the surface mixed layer and deep layer, we use that $c_d \gg c_s$. To find the fast timescale, we approximate that T_d is constant and equal to its initial condition, $\overline{T_d} = T_d^0$, giving the solution to equation (S1):

$$\overline{T_s} = (T_s^0 - T_s^F)\,\exp(-t/\tau_f) + T_s^F\,. \tag{S3}$$

Here, T_s^0 is the initial condition and the steady state solution under forcing F is

$$T_s^F \equiv \frac{\overline{a\,S} - A + B\,T_f + F + k_v T_d^0}{B + k_v}, \tag{S4}$$

with the fast timescale,

$$\tau_f \equiv \frac{c_s}{B + k_v} = 1.6 \text{ years}. \tag{S5}$$

To find the slow time scale, we assume the surface mixed layer is in steady state, $c_s \frac{d\overline{T_s}}{dt} = 0$, which allows us to use equation (S1) to find the surface temperature as a function of $\overline{T_d}$. The gives a solution to equation (S2):

$$\overline{T_d} = (T_d^0 - T_d^F)\,\exp(-t/\tau_s) + T_d^F\,, \tag{S6}$$

where the steady state solution under forcing F is

$$T_d^F = \frac{\overline{a\,S} - A + B\,T_f + F}{B}, \tag{S7}$$

and the slow timescale is

$$\tau_s = \frac{c_d\,(B + k_v)}{k_v B} = 77 \text{ years}. \tag{S8}$$

These take a form analogous to the timescales found in the theoretical model of Held et al. (2010), although they have different values because of the parameters.

In order to consider evolution of the surface temperature on longer timescales, the evolution of the deep layer (S6)-(S8) can be included in the equations for the surface temperature evolution (S3)-(S5) as

$$\overline{T_s} = \frac{k_v F}{B\,(B+k_v)} \exp(-t/\tau_f - t/\tau_s) - \frac{F}{B} \exp(-t/\tau_f) - \frac{k_v F}{B\,(B+k_v)} \exp(-t/\tau_s) + T_s^F. \quad \text{(S9)}$$

This combined analytical approximation describes the annual-mean global-mean surface temperature after the forcing is instantaneously changed by F from an equilibrated model state with $F = 0$. Note that the governing equations for an ice-free climate [Eqs. (S1)-(S2)] can also be solved exactly, which leads to a quantitatively similar but less transparent solution.

These analytical approximations to the solution are compared with the numerical solution in Fig. S1. For ice-free conditions (top four panels), the simple approximate solution for $\overline{T_s}$ (S3)-(S5) agrees well with the numerical solution during the first few e-foldings, and the combined solution (S9) agrees fairly well thereafter. When ice is present, the simulated steady state temperature change under a given change in climate forcing is underestimated by this representation because it does not take into account changes in surface albedo, as shown in Fig. S1 (bottom two panels).

Text S3. Widely Varied Climates.

Both the oceanic mechanism presented in the main text and the surface albedo feedback (SAF) depend on the location of the ice edge. The oceanic mechanism enhances warming in locations where ice is present, whereas the SAF enhances warming only in locations of ice loss. An implication of this is that the SAF would cause the Arctic temperature to change less than the global-mean temperature in cold climates with the sea ice edge residing outside the Arctic, whereas the proposed mechanism would always cause Arctic amplification as long as the Arctic is ice-covered and only a smaller fraction of the global ocean has sea ice. This can be see in Fig. S6, which has PA < 1 for runs with a locked vertical heat flux (yellow) in the coldest simulated climates (with starting values of F below -13 Wm^{-2}), which indicates that the SAF acts against Arctic amplification in these climates. On the other hand, nearly all of the runs with the vertical heat flux free to evolve (orange) have more polar amplification than the locked runs in Fig. S6, which indicates that the ocean heat flux mechanism enhances Arctic amplification in nearly the full range of the simulated climates. There are exceptions to this, however, at both edges of the plot: when the starting values of F is -19 Wm^{-2}, the run with free vertical heat flux transitions into a snowball earth state; and when the starting values of F is greater than 16 Wm^{-2}, there is no sea ice throughout the year and neither process contributes to Arctic amplification.

References

Carmack, E., Polyakov, I., Padman, L., Fer, I., Hunke, E., Hutchings, J., ... Winsor, P. (2015). Toward quantifying the increasing role of oceanic heat in sea ice loss in the new Arctic. *Bulletin of the American Meteorological Society*, *96*(12), 2079-2105. doi: {10.1175/BAMS-D-13-00177.1}

Davis, P. E. D., Lique, C., Johnson, H. L., & Guthrie, J. D. (2016). Competing effects of elevated vertical mixing and increased freshwater input on the stratification and sea ice cover in a changing Arctic Ocean. *Journal of Physical Oceanography*, *46*(5), 1531-1553. doi: {10.1175/JPO-D-15-0174.1}

Flato, G., Marotzke, J., Abiodun, B., Braconnot, P., Chou, S., Collins, W., ... Rummukainen, M. (2013). Evaluation of climate models [Book Section]. In T. Stocker et al. (Eds.), *Climate Change 2013: The Physical Science Basis. Contribution of Working Group I to the Fifth Assessment Report of the Intergovernmental Panel on Climate Change* (pp. 741–866). Cambridge, United

Kingdom and New York, NY, USA: Cambridge University Press. Retrieved from `www.climatechange2013.org` doi: 10.1017/CBO9781107415324.020

Gregory, J. (2000). Vertical heat transports in the ocean and their effect an time-dependent climate change. *Climate Dynamics*, *16*(7), 501-515. doi: {10.1007/s003820000059}

Held, I. M., Winton, M., Takahashi, K., Delworth, T., Zeng, F., & Vallis, G. K. (2010). Probing the fast and slow components of global warming by returning abruptly to preindustrial forcing. *Journal of Climate*, *23*(9), 2418-2427. doi: {10.1175/2009JCLI3466.1}

Hwang, Y.-T., Frierson, D. M. W., & Kay, J. E. (2011). Coupling between Arctic feedbacks and changes in poleward energy transport. *Geophysical Research Letters*, *38*. doi: {10.1029/2011GL048546}

Nummelin, A., Li, C., & Smedsrud, L. H. (2015). Response of Arctic Ocean stratification to changing river runoff in a column model. *Journal of Geophysical Research-Oceans*, *120*(4), 2655-2675. doi: {10.1002/2014JC010571}

Peterson, A. K., Fer, I., McPhee, M. G., & Randelhoff, A. (2017). Turbulent heat and momentum fluxes in the upper ocean under Arctic sea ice. *Journal of Geophysical Research-Oceans*, *122*(2), 1439-1456. doi: {10.1002/2016JC012283}

Polyakov, I. V., Pnyushkov, A. V., Alkire, M. B., Ashik, I. M., Baumann, T. M., Carmack, E. C., ... Yulin, A. (2017). Greater role for Atlantic inflows on sea-ice loss in the Eurasian Basin of the Arctic Ocean. *Science*, *356*(6335), 285+. doi: {10.1126/science.aai8204}

Polyakov, I. V., Pnyushkov, A. V., & Carmack, E. C. (2018). Stability of the Arctic halocline: a new indicator of Arctic climate change. *Environmental Research Letters*, *13*(12). doi: {10.1088/1748-9326/aaecle}

Reigstad, M., Wassmann, P., Riser, C., Oygarden, S., & Rey, F. (2002). Variations in hydrography, nutrients and chlorophyll a in the marginal ice-zone and the central Barents Sea. *Journal of Marine Systems*, *38*(1-2), 9-29. doi: {10.1016/S0924-7963(02)00167-7}

Wagner, T. J. W., & Eisenman, I. (2015). How climate model complexity influences sea ice stability. *Journal of Climate*, *28*(10), 3998-4014. doi: {10.1175/JCLI-D-14-00654.1}

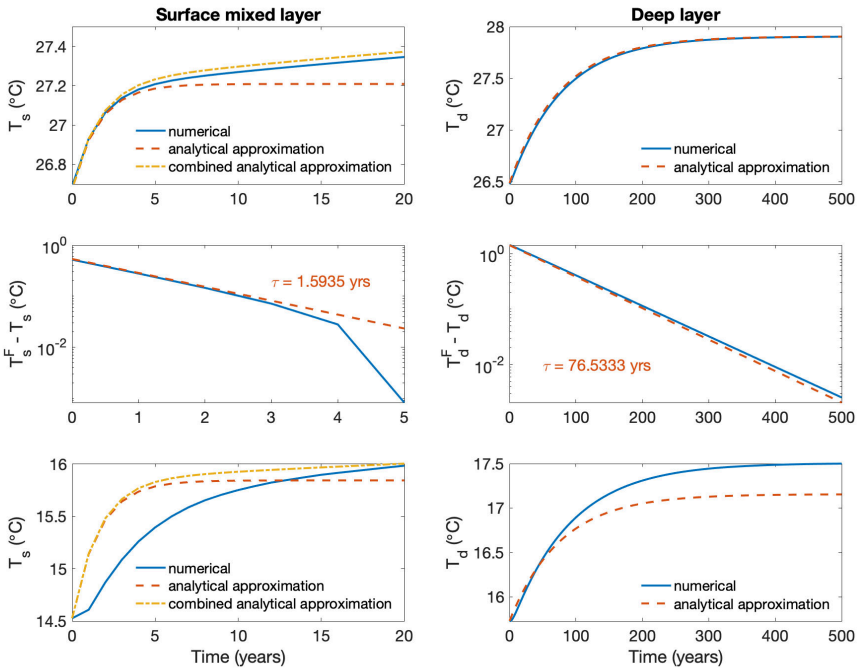

Figure S1. Transient evolution of the annual-mean hemispheric-mean surface mixed layer temperature (left) and deep layer temperature (right). Numerical solutions of the idealized model are shown in solid blue. For the surface mixed layer, the analytical approximation that holds T_d constant [equations (S3)-(S5)] is indicated as an orange dashed line and the combined analytical approximation that includes the evolution of T_d [equation (S9)] is indicated as a yellow dash-dotted line. For the deep layer, the analytical approximation that uses a steady-state approximation for T_s [equations (S6)-(S8)] is indicated as an orange dashed line. The top four panels are for a simulated climate that is sufficiently warm to be completely ice-free. In the top two panels, the analytical solutions provide fairly accurate approximations to the numerical solutions. Note that after several centuries, when the deep layer temperature is approximately in steady state, the combined analytical solution for T_s matches the numerical solution (not shown). In the middle two panels, the departure of each temperature from it's final steady-state value is plotted using log-linear axis scaling, such that exponential decay appears linear with a slope given by the inverse of the decay timescale τ. The bottom panel shows numerical results and the analytical approximation in the default climate, which has sea ice in high latitudes. In this case the analytical solutions do not capture the changes in albedo, which leads to an underestimation of the final steady-state temperature and an overestimation of the rate at which the surface temperature initially responds.

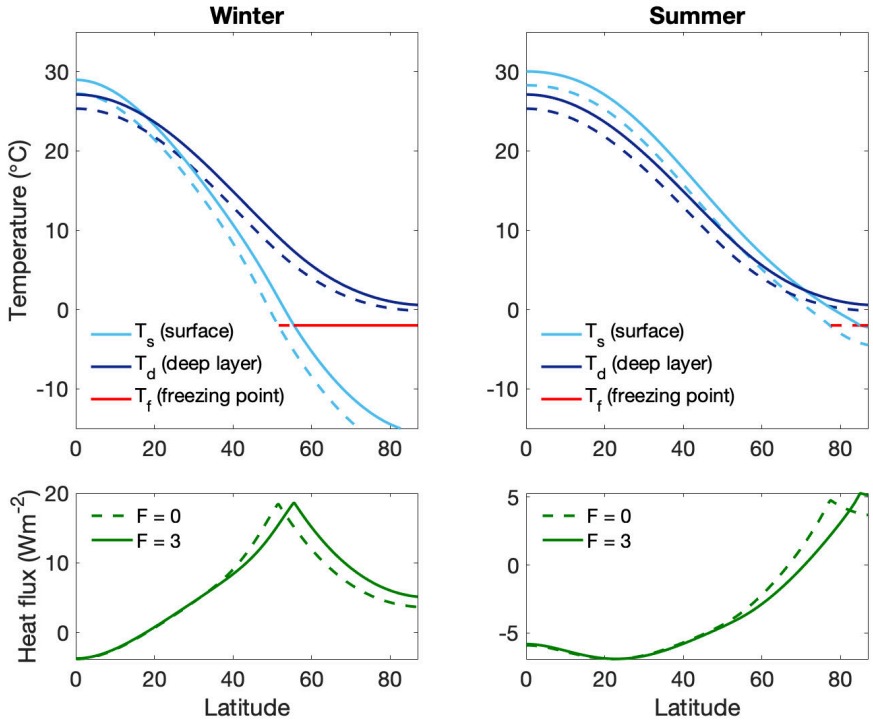

Figure S2. Temperature and vertical heat flux profiles plotted against latitude for midwinter (left, $t = 0.25$) and midsummer (right, $t = 0.75$). Dashed lines indicate the simulated climate with $F = 0$ Wm^{-2} and solid lines indicate $F = 3$ Wm^{-2}. In the top panels, the surface temperature is in light blue, the deep layer temperature is in dark blue, and the freezing point is in red. The bottom panels show the vertical heat flux between the two layers, which is proportional to the difference between the surface mixed layer and deep layer temperatures. Note the surface mixed layer temperature is set to either the surface temperature (light blue) or the freezing point (red) depending whether or not ice is present (i.e., whether the surface temperature is less than the freezing point).

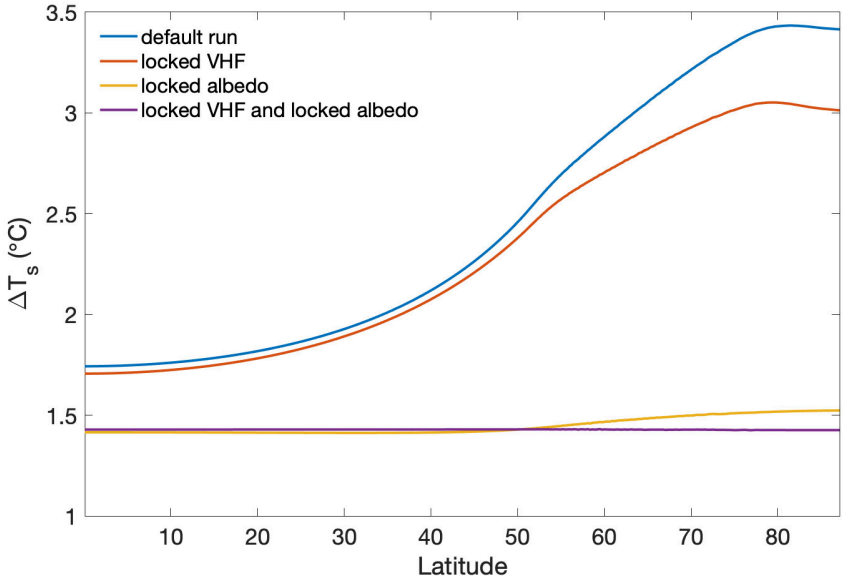

Figure S3. Annual-mean surface temperature difference between simulated steady-state climates with $F = 3$ Wm^{-2} and $F = 0$ Wm^{-2}. The blue and orange lines are equivalent to what is plotted in Fig. 3b in the main text (solid and dash-dotted green lines, respectively). Here, the yellow line shows the case when only the albedo is locked, and the purple line shows the case when both the albedo and the vertical heat flux (VHF) are locked (in which case there is no polar amplification as expected). It can be seen that if the contributions from the surface albedo alone (orange line) and VHF alone (yellow line) are linearly added, they do not sum to the total polar amplification shown in blue. This suggests there is a nonlinear contribution from the interaction between the VHF and the surface albedo.

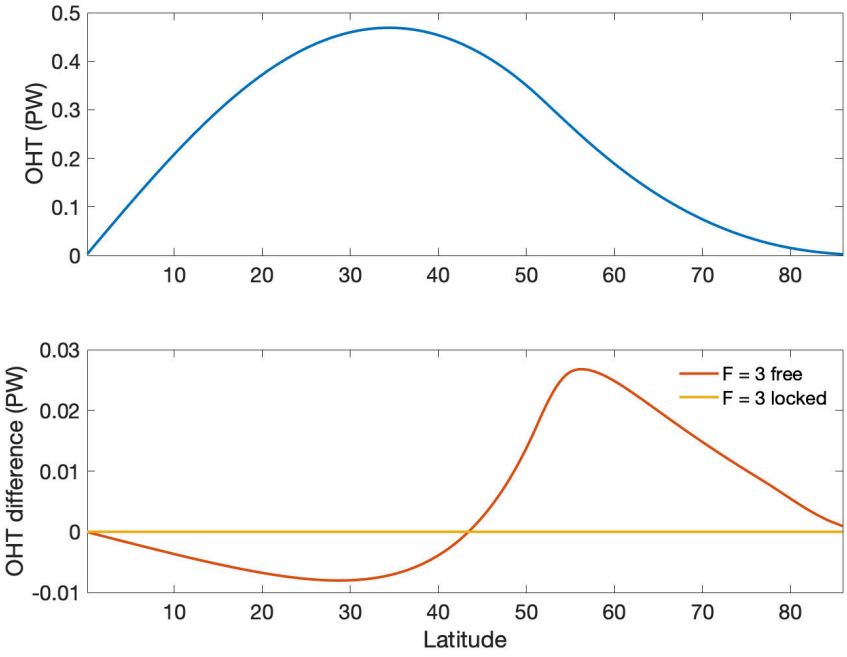

Figure S4. Annual-mean ocean heat transport (OHT). The top panel shows annual-mean OHT for the default climate scenario ($F = 0$ Wm^{-2}). The difference between the default climate case and the warmed climate cases ($F = 3$ Wm^{-2}) is plotted in the bottom panel, where simulations using the default model configuration are shown in orange ("free"), and simulations with the vertical heat flux locked to match the initial climate are shown in yellow ("locked"). Since OHT does not change in the locked case, the yellow line is at 0 PW. In the free case, the increase in OHT into the polar region (at 70 °N) is 0.015 PW, or 0.007 PW per degree of hemispheric warming. This value falls within the range of GCM projections, as discussed in the main text, although the maximum increase in OHT occurs at a more southward location than in most GCMs (Hwang et al., 2011). Note however that these results include only heat transport in the depth range 200–800 m, and the idealized model does not include representations of the Atlantic Meridional Overturning Circulation and a range of other processes that influence total heat transport in the global ocean, so the simulated OHT plotted here is not expected to closely match the global distribution of zonally–integrated depth–integrated OHT typically found in GCMs and observational estimates (e.g., Flato et al., 2013).

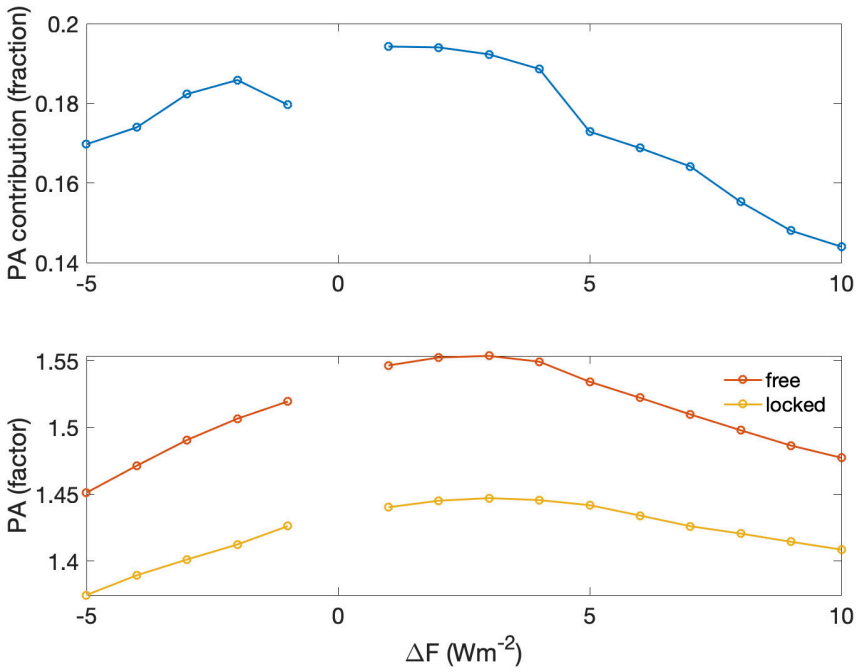

Figure S5. Sensitivity of polar amplification (PA) to the change in climate forcing for simulations starting at $F = 0$ and ending at $F = \Delta F$. The bottom panel shows PA for simulations using the default model configuration in orange ("free"), and simulations with the vertical heat flux locked to match the initial climate in yellow ("locked"). Note that PA is not defined for $\Delta F = 0$. The top panel shows the corresponding contribution to PA, $\mathrm{PA}_{contribution}$, which is given in equation (13) of the main text. Note that after warming of at least $\Delta F = 4$ Wm^{-2}, the Arctic is seasonally ice-free; this is the range where the PA values start to decrease in the bottom panel. With negative forcing ($\Delta F < 0$), the model is being cooled and polar amplification refers to enhanced cooling rather than enhanced warming. In this scenario, the vertical heat fluxes are still contributing to polar amplification.

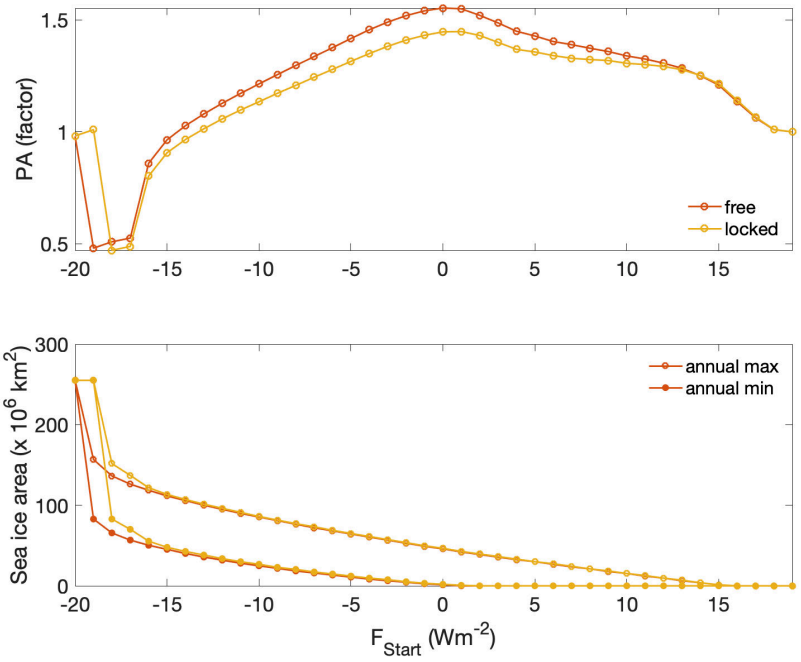

Figure S6. Sensitivity of polar amplification (PA) to the initial climate. The model is initially run to steady state under forcing F_{Start}, and then the forcing is increased by $\Delta F = 3$ Wm^{-2} and the model is run until it again reaches steady state. The top panel shows the level of PA associated with the difference between the two steady-state climates. Simulations using the default model configuration are shown in orange ("free"), and simulations with the vertical heat flux locked to match the initial climate are shown in yellow ("locked"). The bottom panel shows the annual minimum (closed circles) and maximum (open circles) sea ice area after warming by ΔF = 3 Wm^{-2} for the range of values of F_{Start}. Note the transitions at F_{Start} = 1 Wm^{-2}, when the warmer steady state has only seasonal ice, and at F_{Start} = 4 Wm^{-2}, when the initial climate has only seasonal ice, which are most evident in the top panel. In the colder climates, there is a jump to a completely ice-covered hemisphere (snowball earth) at $F_{\text{Start}} = -19$ and -20 for the locked and free cases, respectively. Note that here the PA is not exactly at one as the system is not in steady state in the simulated snowball earth. At $F_{\text{Start}} = 19$, both runs becomes completely ice-free throughout the year, and there is no polar amplification in the model (PA = 1).

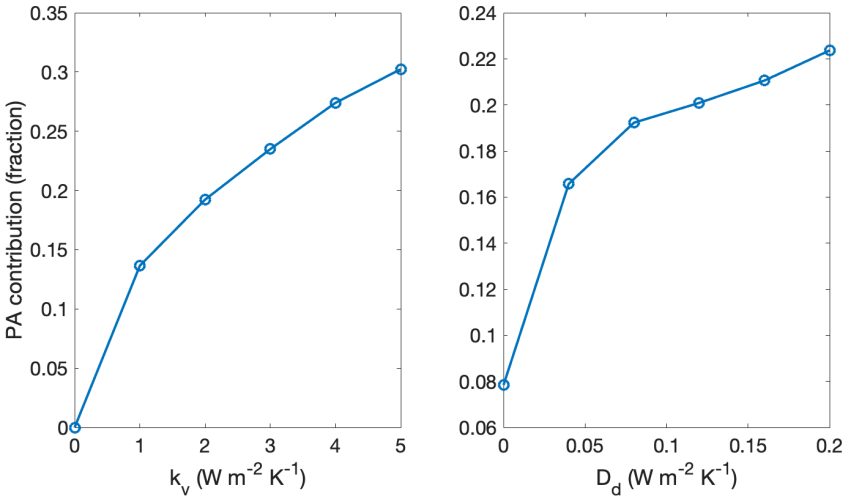

Figure S7. Sensitivity of polar amplification (PA) to model parameters when F is increased from 0 Wm^{-2} to 3 Wm^{-2}. Fractional contribution to PA [$\mathrm{PA}_{contribution}$, given in equation (13) of the main text] for changes in the model parameters k_v, which is related to the insulating effect of the halocline, and D_d, which is related to horizontal heat transport in the deep layer. (left) All model parameters are fixed at the default values except k_v which is varied between 0 and 5, with the default value being 2. (right) All model parameters are fixed at the default values except D_d which is varied between 0 and 0.2, with the default value being 0.08. Note that the PA contribution is not zero when D_d is zero, which is due to the interaction between the surface albedo and the seasonal cycle of the vertical heat flux in the model: even without horizontal transport in the deep layer, heat can still enter the deep layer in ice-free areas during the summer and be released under ice in winter. Note also that the initial climate varies with the parameter values, which is not explicity taken into account here.

Table 1. Model parameters and values

Parameter	Description	Value
A	OLR reference value (W m^{-2})	189
a_0	Ice-free coalbedo at equator	0.7
a_2	Ice-free coalbedo spatial dependence	0.1
a_i	Ice-covered coalbedo	0.4
B	OLR temperature dependence (W $m^{-2}K^{-1}$)	2.1
c_d	Deep layer heat capacity (W yr $m^{-2}K^{-1}$)	78.4
c_s	Surface mixed layer heat capacity (W yr $m^{-2}K^{-1}$)	6.53
D_d	Coefficient for horizontal heat transport in deep layer (W $m^{-2}K^{-1}$)	0.08
D_s	Coefficient for horizontal heat transport in atmosphere (W $m^{-2}K^{-1}$)	0.5
F	Climate forcing (W m^{-2})	0 (varies)
k	Sea ice thermal conductivity (W $m^{-1}K^{-1}$)	2
k_v	Vertical heat flux coefficient (W $m^{-2}K^{-1}$)	2
L_f	Sea ice latent heat of fusion (W yr m^{-3})	9.5
S_0	Insolation at equator (W m^{-2})	420
S_1	Insolation seasonal dependence (W m^{-2})	355
S_2	Insolation spatial dependence (W m^{-2})	240
T_f	Freezing temperature (°C)	−2